INTERNATIONAL JOURNAL FOR NUMERICAL METHODS IN FLUIDS
Int. J. Numer. Meth. Fluids 2003; **41**:1147–1172 (DOI: 10.1002/fld.484)

Development of an optimal hybrid finite volume/element method for viscoelastic flows

M. Aboubacar and M. F. Webster*,†

Institute of Non-Newtonian Fluid Mechanics, Department of Computer Science, University of Wales, Swansea, Singleton Park, Swansea SA2 8PP, U.K.

SUMMARY

A cell-vertex hybrid finite volume/element method is investigated that is implemented on triangles and applied to the numerical solution of Oldroyd model fluids in contraction flows. Particular attention is paid to establishing high-order accuracy, whilst retaining favourable stability properties. Elevated levels of elasticity are sought. The main impact of this study reveals that switching from quadratic to linear finite volume stress representation with discontinuous stress gradients, and incorporating local reduced quadrature at the re-entrant corner, provide enhance stability properties. Solution smoothness is achieved by adopting the non-conservative flux form with area integration, by appealing to quadratic recovered velocity-gradients, and through consistency considerations in the treatment of the time term in the constitutive equation. In this manner, high-order accuracy is maintained, stability is ensured, and the finer features of the flow are confirmed via mesh refinement. Lip vortices are observed for $We > 1$, and a trailing-edge vortex is also apparent. Loss of evolution and solution asymptotic behaviour towards the re-entrant corner are also discussed. Copyright © 2003 John Wiley & Sons, Ltd.

KEY WORDS: hybrid finite volume/element; cell-vertex

1. INTRODUCTION

This study considers the accuracy and stability properties of a new hybrid finite volume/element scheme in its application to the numerical solution of viscoelastic contraction flows. Previously, a second-order scheme has been constructed that demonstrates its efficiency over finite element counterparts on model problems. The current direction of investigation focuses on highly elastic solutions, with retention of accuracy and favourable stability properties. Holding this goal in mind, this article presents results for the benchmark problem of flow through a 4:1 planar contraction with sharp re-entrant corners for an Oldroyd-B model.

* Correspondence to: M. F. Webster, Institute of Non-Newtonian Fluid Mechanics, Department of Computer Science, University of Wales, Swansea, Singleton Park, Swansea SA2 8PP, U.K.
† E-mail: m.f.webster@swansea.ac.uk

Contract/grant sponsor: European TMR Network on "Dynamics of Polymeric Liquids": contract/grant number: FMRX-CT98-0210

Received 18 May 2002
Revised 24 June 2002

A comprehensive literature review on this problem may be found in Matallah *et al.* [1] with further detail in Matallah [2], White *et al.* [3], Baaijens [4] and Walters and Webster [5].

Typically, incompressible viscoelastic flows may be classified through mixed parabolic-hyperbolic differential systems. The central ethos of the current approach is to apply finite element (fe) technology to the self-adjoint sections of the system (optimal), and finite volume (fv) schemes to the hyperbolic parts. Finite volume technology has advanced considerably, over the last decade, in its treatment of pure advection equations, and has matured sufficiently to attack the viscoelastic regime. In this regard, we may cite the important contributions of Morton and co-workers [6, 7], Struijs *et al.* [8] and Tomaich and Roe [9], that have advocated cell-vertex fv formulations for advection, Euler and compressible Navier–Stokes equations. For cell-centred counterparts, see Berzins and Ware [10]. Generally, cell-vertex formulations require considerably less degrees of freedom than cell-centred forms, depending upon narrower stencils. In the viscoelastic context, the emergence of non-trivial source terms, via the constitutive equations, gives rise to some open questions for finite volume representations. In fact, in shear flow or in the vicinity of no-slip boundaries, flux terms vanish and source terms dominate. Such stress source terms display dependence on stress and velocity gradients, and their treatment is addressed comprehensively in this study.

Features of the current hybrid approach include a time-stepping procedure that combines a finite element discretization (semi-implicit Taylor–Galerkin/pressure-correction) for continuity and momentum equations, and a cell-vertex finite volume scheme for the constitutive equation. The combination is posed as a fractional-staged formulation based upon each time-step. The positioning of finite volume nodal values and control volumes, is such that four linear finite volume triangular cells are formed as embedded sub-cells of each parent quadratic finite element triangular cell (note association with superconvergence points, see recovery in Matallah *et al.* [1]). Sub-cell reference has arisen earlier in the fe literature, see for example, the SU method implementation of Marchal and Crochet [11]. Here, this is accomplished by connecting the mid-side nodes of the parent finite element triangular cell. An important aspect is that with stress variables located at the vertices of the finite volume cells, no interpolation is required to recover the finite element nodal stress values. The cell-vertex approach is naturally associated with fluctuation distribution, an upwinding technique that distributes control volume contributions for each equation to provide nodal solution updates. The consideration of triangular cells offers the flexibility of either structured or unstructured meshing as equally viable options, without further complication.

The literature on fv implementations for viscoelastic flow divides into two camps: those dealing with a full system through fv and hybrid versions, see Reference [12] for review. Most consider established standard low-order discretization, with cell-centred or staggered grid systems, and SIMPLER-type algorithms for steady-state solutions on structured rectangular grids. Essentially, this implies piecewise constant interpolation. There, principal attention has been directed towards highly elastic solutions, often to the detriment of establishing accuracy in this complicated scenario. Two recent papers adopting this approach for the abrupt 4:1 planar contraction flow are those of Phillips and Williams [13] and Alves *et al.* [14]. Phillips and Williams used a semi-Lagrangian method to simulate the flow of an Oldroyd-B fluid, with and without the inclusion of inertia. This is a first-order implementation that applies a semi-Lagrangian treatment for convection terms and uses a staggered grid, that avoids the calculation of normal stresses at the re-entrant corner. Only the shear stress variable is located at the corner singularity, though an averaging procedure is invoked, replacing the corner value by

shear stress values at cross-stream and upstream neighbouring nodes. These authors assessed accuracy by demonstrating that the size of the salient-corner vortex remained fairly constant with mesh refinement, and concurred with Matallah *et al.* [1] and Sato and Richardson [15], both for creeping flow and with inertia ($Re = 1$). Phillips and Williams commented upon the absence of lip–vortex activity for coarse meshes, and on their finest mesh, its appearance around $We = 2$ with growth as the level of fluid elasticity increases up to a maximum value of $We = 2.5$. In contrast, Alves *et al.* considered the same flow for an upper-convected Maxwell (UCM) fluid, comparing both first-order and second-order schemes, again using staggered grid systems. However, unlike with the study of Phillips and Williams, none of the stress components are located at the re-entrant corner. A first-order implementation was able to converge up to $We = 8$ on a refined mesh (third in a series of four, consecutively refined meshes), but proved inaccurate, reflecting large spurious vortex structure. An alternative second-order scheme failed to converge at Weissenberg numbers above unity on the same refined mesh. Alves *et al.* related this premature breakdown of numerical convergence (inhibiting advance in We) to oscillations in the stress field, associated with the use of high-order upwinding in regions of high stress gradients. Therefore, these authors invoked, in conjunction with their second-order scheme, a limiting (min-mod) procedure applied to the stress convection (see also, Sato and Richardson [15]). In this manner, Alves *et al.* were able to reach a Weissenberg number of five on their third finest mesh, and three on their fourth, most fine mesh. Relevant issues that arise in Reference [14] can be summarized as follows: diminishing lip-vortex with mesh refinement as reported by Matallah *et al.* [1], and Xue *et al.* [16]; lip-vortex growth (see References [1, 13] to a lesser extent), and diminishing salient-corner vortex with increasing elasticity; agreement with the asymptotic behaviour of velocities and stresses near the re-entrant corner, as predicted theoretically by Hinch [17] for an Oldroyd-B fluid (see also, Renardy [18, 19] for an UCM fluid). The present article develops these themes somewhat further.

The methodology proposed behind the present cell-vertex finite volume scheme is novel in this domain and addresses both accuracy and stability behaviour, along with calculating stress fields in the presence of a singularity. Consistent treatment for stress flux and source terms is maintained, reminiscent of fe Petrov–Galerkin variational weighting (supg). Likewise, such considerations may be extended to embrace the transient terms involved. The hybrid scheme of Sato and Richardson [15] deserves some mention, bearing resemblance to the present. In contrast, this scheme employed a time-explicit fe method for momentum and time-implicit fv for pressure and stress of cell-centred type. Higher-order upwinding was achieved through application of a TVD flux-corrected transport scheme to the advection terms of the stress equation. Clearly, some attempt must be made to address the complications of flux-source interaction, and to accommodate for highly elastic convection, when this arises. In this respect, the direction adopted by Tanner, Phan-Thien and co-workers [20, 21] was to incorporate a stabilizing artificial stress diffusion, reminiscent of the SU method of Marchal and Crochet [11]. The fe studies of Baaijens [22, 23] consider various alternative Galerkin least-squares stabilization procedures, including strain-rate stabilization. The discontinuous Galerkin aspects involved, strive for low-order stress interpolation and gain stability accordingly. There, the correspondence to fv weighting and the localized treatment of solution has similar characteristics to the present approach. Under such discontinuous stress representation on a global scale, we also note the work of Fortin and Fortin [24] with discontinuous quadratic interpolation and Basombrío *et al.* [25] with discontinuous linear interpolation.

Fluctuation splitting schemes, natural to the cell-vertex treatment, may be of linear or non-linear type, and introduce such properties as positivity and linearity preservation. To date, various forms have been considered and their properties analysed [12], recognizing the importance of linearity preservation to achieve high-order accuracy. Our prior studies established accuracy properties against analytical solutions for smooth flows [12], before addressing stability issues for complex smooth and non-smooth flows [26]. Here, we extend and revise our methodology with complex flows and accuracy in mind.

We identify the relative strengths and weaknesses of various strategies for dealing with flux and source terms. For the stress nodal update, we consider a fluctuation distribution contribution over the fv-triangle, and a uniform distribution over the median dual cell. The latter is a unique non-overlapping region associated with each finite volume node, a new concept arising with cell-vertex schemes. Other issues covered concern, the use of conservative/non-conservative stress flux treatment (area or line integrals), the choice of stress representation, the order and continuity of stress gradient and velocity gradient representations, the treatment of the re-entrant corner solution, and time consistency. The corresponding properties of the schemes considered are adjudged, identifying solution behaviour (particularly in stress profiles), as a consequence of scheme implementation.

2. GOVERNING EQUATIONS

Incompressible viscoelastic flows are governed by conservation laws for mass and momentum and a constitutive equation for stress. In non-dimensional form, the balance equations for isothermal flows read

$$\nabla \cdot \boldsymbol{u} = 0 \tag{1}$$

$$Re\frac{\partial \boldsymbol{u}}{\partial t} = -Re\,\boldsymbol{u}\cdot\nabla\boldsymbol{u} - \nabla p + \nabla\cdot\left(2\frac{\mu_s}{\mu}\boldsymbol{d} + \boldsymbol{\tau}\right) \tag{2}$$

and the constitutive equation for an Oldroyd-B fluid may be expressed as

$$We\frac{\partial \boldsymbol{\tau}}{\partial t} = -We\,\boldsymbol{u}\cdot\nabla\boldsymbol{\tau} - \boldsymbol{\tau} + 2\frac{\mu_e}{\mu}\boldsymbol{d} + We(\boldsymbol{L}\cdot\boldsymbol{\tau} + \boldsymbol{\tau}\cdot\boldsymbol{L}^{\mathrm{T}}) \tag{3}$$

where $\boldsymbol{u}$, p, $\boldsymbol{\tau}$ represent the fluid velocity, the hydrodynamic pressure and the extra-stress tensor. The total viscosity μ is split into Newtonian (μ_s) and polymeric (μ_e) contributions, such that $\mu = \mu_s + \mu_e$; $\boldsymbol{d} = (\boldsymbol{L} + \boldsymbol{L}^{\mathrm{T}})/2$ represents the Euler rate-of-deformation tensor and $\boldsymbol{L}^{\mathrm{T}} = \nabla\boldsymbol{u}$, the velocity gradient.

The Reynolds and Weissenberg numbers are defined according to convention as

$$Re = \frac{\rho UL}{\mu}, \quad We = \frac{\lambda U}{L} \tag{4}$$

where ρ, λ are the fluid density and relaxation time and U, L are characteristic velocity (average at outlet) and length scale (channel exit half-width) of the flow. Creeping flow is assumed throughout and, as such, the momentum convection terms are discarded, whilst transient terms are retained to provide the time-stepping facility, see Carew *et al.* [27].

3. PROBLEM SPECIFICATION

The benchmark problem of flow through an abrupt 4:1 planar contraction with a re-entrant corner for an Oldroyd-B fluid is known to be a formidable test problem, in terms of stability at high Weissenberg number. It is equipped with an analytical representation for the corner solution and is well-documented in the literature. Therefore, it is a natural choice in this numerical study. In a subsequent article [28], we go further to address more robust and physically representative constitutive models, and complex smooth flows such as contraction flow with a rounded corner.

Figure 1 displays the set of structured triangular meshes employed, showing zoomed sections around the re-entrant corner, following hierarchical refinement based on zonal mesh density in the contraction region. M1, M2 and M3 have been successfully utilized earlier by Matallah *et al.* [1] to demonstrate solution convergence with mesh refinement for the fe/supg scheme. This offers a convenient reference point to qualify the various fv strategies. Here, we refine further generating the hybrid NM3 mesh. In contrast to M3, NM3 mesh displays increased refinement in the salient-corner region, but also has one quarter of the element size in the immediate corner vicinity and one-half just beyond. This choice allows us to discern vortex activity more clearly in this critical region. Table II displays the mesh characteristics. As

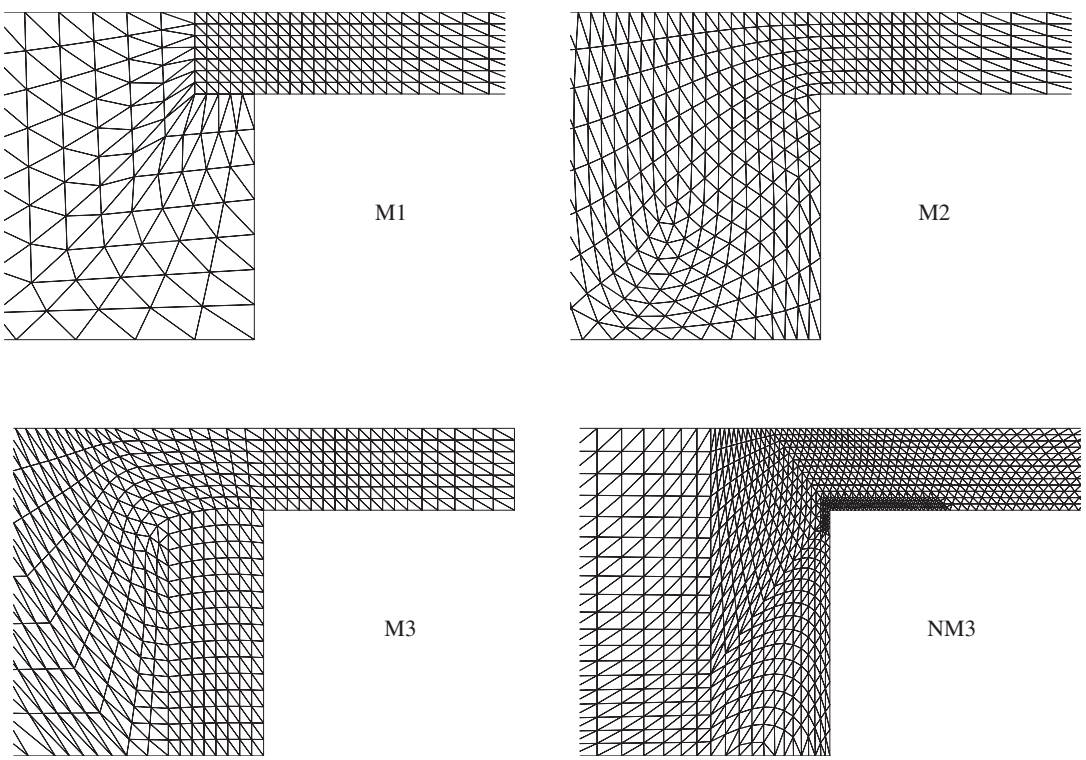

Figure 1. Set of meshes: zoomed section around re-entrant corner.

Table I. Table of schemes; for $\boldsymbol{u}$, $\nabla\boldsymbol{u}$, $\boldsymbol{\tau}$, and $\nabla\boldsymbol{\tau}$: 2, 1, and 0 quadratic, linear and constant representation, respectively; Rec. (recovered) and Mul. (multi-valued options); Γ (line) and Δ (area) integral; C.R.I. (Corner reduced integration).

Scheme	$\boldsymbol{u}$	$\nabla\boldsymbol{u}$	$\boldsymbol{\tau}$	$\nabla\boldsymbol{\tau}$	$\int R_T$	CT	C.R.I.	We_{crit} – M2
FV0	2	1 Rec.	2	1 Rec.	Γ	CT_0	$\times$	1.1
FV1	2	1 Rec.	1	0 Rec.	Γ	CT_0	$\times$	1.6
FV1.1	2	1 Rec.	1	0 Rec.	Γ	CT_1	$\times$	1.7
FV1.2	2	1 Rec.	**1**	**0 Rec.**	Γ	CT_2	$\times$	2.0
FV2	2	1 Rec.	2	1 Rec.	Δ	CT_2	$\times$	0.3
FV2.1	2	1 Rec.	1	0 Rec.	Δ	CT_2	$\times$	0.8
FV3	2	1 Rec.	**1**	**0 Mul.**	Δ	CT_2	$\times$	3.0
FV4	2	2 Rec.	1	0 Mul.	Δ	CT_2	$\times$	2.4
FV4.1	2	**2 Rec.**	1	0 Mul.	Δ	CT_2	$\surd$	3.7

before, the inlet and outlet lengths are $27.5L$ and $49L$ to ensure fully developed flows in these regions, L being the half-width of the downstream channel.

By convention, we apply no-slip boundary conditions at the wall and enforce symmetry at the centerline. Velocity is imposed at the inlet and exit through Waters and King transient boundary conditions [29]. These are analytical transient conditions for the Oldroyd model, representing a one-dimensional local solution. The pressure is held fixed at a single exit point to remove the indeterminacy of pressure level. We have appealed to a point-wise time-dependent initial-value solution for inlet stresses, obtained by imposing vanishing stress flux and kinematics as above. In this manner, we have reduced the CPU time consumption by 25%, without degradation in the steady-state solution. The non-dimensional parameters are $\mu_e/\mu = 8/9$, $\mu_s/\mu = 1/9$ and $Re = 0$ (creeping flow). Typical time steps are $0(10^{-3})$ and five Jacobi iterations are employed for the fe stages. The time-stepping termination criteria is taken as 10^{-5}, a relative solution temporal increment within a least squares measure [1, 12]. To investigate the stability behaviour of the various scheme alternatives summarized in Table I, we commence each simulation at $We = 0.1$ from a quiescent initial state in all field variables and increment the Weissenberg number by 0.1, till the scheme fails to converge (encountering either temporal oscillations or numerical divergence).

4. BACKGROUND TO METHODOLOGY

4.1. Numerical framework

We recall briefly the algorithmic structure upon which both the fe and hybrid fe/fv are articulated. The reader is referred to Matallah *et al.* [1] and Wapperom and Webster [12] for detailed discussion on these methodologies.

One may commence with the structure of the fe scheme, and point to the hybrid fe/fv options in contrast. The general scheme follows a time-splitting semi-implicit formulation. There are two distinct aspects to this approach: a Taylor–Galerkin scheme and a pressure-correction scheme. The Taylor–Galerkin scheme is a two-step Lax–Wendroff time stepping procedure, extracted via a Taylor series expansion in time [30, 31]. The pressure-correction

method accommodates the incompressibility constraint to ensure second-order accuracy in time (see References [32, 33]). This leads to a three-stage structure for each time step that can be stated in discrete form as follows [26]:

Stage 1a.

$$\frac{2}{\Delta t}A_u(\mathscr{U}^{n+1/2}-\mathscr{U}^n)=b_u(\mathscr{P}^n,\mathscr{U}^n,\mathscr{T}^n,\mathscr{D}^n)$$
$$\frac{2We}{\Delta t}A_\tau(\mathscr{T}^{n+1/2}-\mathscr{T}^n)=b_\tau(\mathscr{U}^n,\mathscr{T}^n,\mathscr{D}^n)$$

Stage 1b.

$$\frac{1}{\Delta t}A_u(\mathscr{U}^*-\mathscr{U}^n)=b_u(\mathscr{P}^n,\mathscr{U}^n,\mathscr{U}^{n+1/2},\mathscr{T}^{n+1/2},\mathscr{D}^{n+1/2})$$
$$\frac{We}{\Delta t}A_\tau(\mathscr{T}^{n+1}-\mathscr{T}^n)=b_\tau(\mathscr{U}^{n+1/2},\mathscr{T}^{n+1/2},\mathscr{D}^{n+1/2}) \tag{5}$$

Stage 2.

$$\frac{\Delta t}{2}A_2(\mathscr{P}^{n+1}-\mathscr{P}^n)=b_2(\mathscr{U}^*)$$

Stage 3.

$$\frac{2}{\Delta t}A_3(\mathscr{U}^{n+1}-\mathscr{U}^*)=b_3(\mathscr{P}^n,\mathscr{P}^{n+1})$$

where the superscript ^{n} denotes the time level, Δt the time step and $\mathscr{U},\mathscr{U}^*,\mathscr{P},\mathscr{T},\mathscr{D}$ the nodal values of velocity, non-solenoidal velocity, pressure, extra-stress and velocity gradient, respectively. A_u, A_2, A_3 are the standard velocity, stiffness and mass matrices. The precise form of A_τ depends on the implementation (fe or hybrid fe/fv), as discussed in the following sections.

The momentum equation in Stage 1, the pressure-correction in Stage 2 and the incompressibility constraint in Stage 3 are discretised spatially via a Galerkin finite element method. For reasons of accuracy, the resulting Galerkin Mass matrix-vector equations at Stages 1 and 3 are solved using an efficient element-by-element Jacobi scheme, requiring only a handful of iterations. A direct Choleski decomposition procedure is invoked to handle Stage 2. Finally, the diffusive terms in Equation (2) are treated in a semi-implicit manner in order to enhance stability.

The parent fe mesh element is a triangular cell with three vertices and three mid-side nodes. To solve for the momentum and continuity equations, the velocity is represented by quadratic shape functions, using the six nodal values, and the pressure by linear functions from the vertices alone, see Figure 2(a). All the above features are common to both fe and hybrid fe/fv implementations. The fe and fv representations depart in their spatial discretization of the stress constitutive equation (see on). The fv sub-cell is an internal triangle of each fe triangle, built on the mid-side node connections. Representation of stress upon each sub-cell may be taken in a variety of ways, including linear on the sub-cells or quadratic from the parent fe cell. These are crucial aspects expanded upon below.

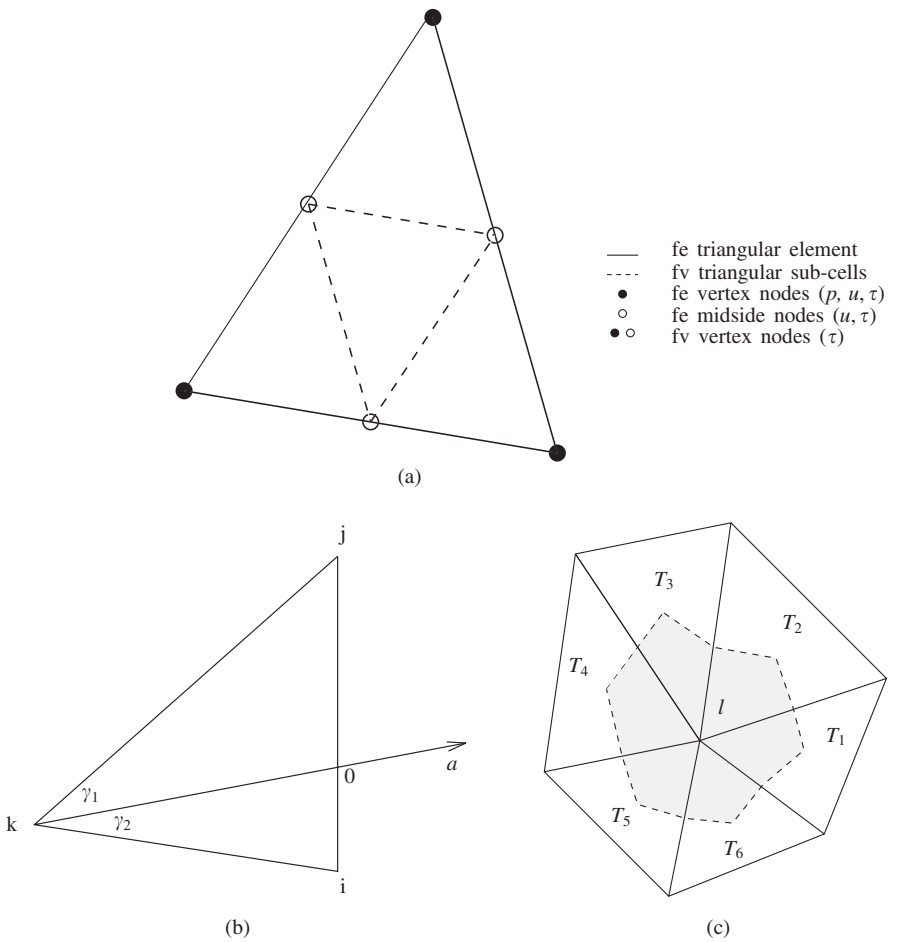

Figure 2. Hybrid finite element/finite volume spatial discretization: (a) Schematic diagram: fe-cell with four fv sub-cells; (b) LDB-scheme, defining γ_1 and γ_2 in fv cell; (c) Control volume about node l,with median dual cell (MDC).

4.2. Finite element method

In this instance with fe discretization of stress, quadratic interpolation functions are used for both velocity and stress, and the matrix $A_{\boldsymbol{\tau}}$ is sparse. Therefore the resulting equation is similar in structure to that of the momentum equation and is solved accordingly. Other features are the incorporation of supg weighting and recovery of velocity gradients (as coefficients of the constitutive equation) that are found necessary to enhance stability of convergence [1, 26]. Here, recovery of velocity gradients implies gathering continuous representations, that themselves depend upon superconvergent recovered nodal values for these quantities. This implementation (fe/supg) has proved successful in reaching high *We*-solutions for the present 4:1 contraction flow and compares favourably with the extensive literature available on the subject, see Matallah *et al.* [1] for review and discussion thereon. Nevertheless, the fe implementation suffers a

heavy computational overhead when compared to its hybrid fe/fv counterpart, as reported in our previous communications [12, 26]. We demonstrate below the superior properties of our optimized hybrid fe/fv scheme above fe/supg, re accuracy and stability on finer meshes.

4.3. *Hybrid finite volume method*

For clarity of the exposé, we summarize the key features of our base hybrid fe/fv method, which has been extensively documented in the precursor papers of Wapperom and Webster [12, 26]. In this implementation, the matrix $A_{\boldsymbol{\tau}}$ is the identity matrix, the need to resolve a matrix-vector equation is avoided, and the right-hand side vector b_u is straightforward to construct. These two features have led to a hybrid fe/fv implementation that is up to five times more efficient than fe/supg for viscoelastic flow past a cylinder and the abrupt 4:1 contraction problem.

Cell-vertex fluctuation distribution (FD) schemes, which are the foundation of the present fv implementation, require only the vertices of a triangular cell to evaluate the solution of a given scalar field. The theory associated with the variants of such FD-schemes is centred around appropriate discretisation choices for pure advection equations. They feature such properties as:

- *Conservation*: that requires the distribution coefficients α_l^{T} to sum to unity for each triangle T, the summation running over its three vertices l.
- *Linearity preservation*: that is associated with second-order accuracy at steady state.
- *Positivity*: that is related to accuracy in the transient development, prohibiting the occurrence of new extrema in the solution. Particular attention must be paid to the issue of dealing with sources, as these may lead to physical extrema, that should not be suppressed artificially by imposing positivity.

Furthermore, FD schemes can be divided into linear and non-linear classes. Non-linear schemes may be both linearity preserving and positive; alternatively, linear schemes can only possess one such property. Since we are interested in viscoelastic flows where sources can be dominant, from our previous experience we have selected the low diffusion B (LDB) scheme. This is a linear scheme with linearity preserving properties, that has proven efficient in dealing with model problems, as well as some complex flows [12, 26]. The LDB distribution coefficients α_i are defined per cell node i according to the angles γ_1 and γ_2 in the fv triangle, subtended on both sides of the cell advection velocity $\boldsymbol{a}$ (an average vector per cell, see Figure 2(b)). The LDB coefficients are defined as

$$\begin{aligned} \alpha_i &= (\sin\gamma_1 \cos\gamma_2)/\sin(\gamma_1+\gamma_2) \\ \alpha_j &= (\sin\gamma_2 \cos\gamma_1)/\sin(\gamma_1+\gamma_2) \\ \alpha_k &= 0 \end{aligned} \tag{6}$$

We point out that the closer the advection velocity $\boldsymbol{a}$ is to being parallel to one of the cell boundaries, the larger the contribution to the downstream node at that boundary, hence minimizing the introduction of spurious numerical diffusion.

To avoid interpolation when recovering the stress nodal values for the momentum equation, the finite volume tessellation is constructed from the finite element grid by connecting the mid-side nodes. This generates four triangular fv sub-cells per fe parent triangle, as indicated

in Figure 2(a). Accordingly, the stresses are computed on the vertices of the fv cells as outlined below.

First, we recast the stress constitutive equation (3) in conservative form,

$$\frac{\partial \tau}{\partial t} = -\nabla \cdot \mathscr{R} + \boldsymbol{Q} \tag{7}$$

$$\mathscr{R} = \boldsymbol{u}\boldsymbol{\tau} \tag{8}$$

$$\boldsymbol{Q} = \frac{1}{We}\left(2\frac{\mu_e}{\mu}\boldsymbol{d} - \boldsymbol{\tau}\right) + \boldsymbol{L}\cdot\boldsymbol{\tau} + \boldsymbol{\tau}\cdot\boldsymbol{L}^{\mathrm{T}} \tag{9}$$

where $\mathscr{R}$ and $\boldsymbol{Q}$ are the flux and the source terms, respectively.

Next, we consider each scalar stress components, $\boldsymbol{\tau}$, acting on an arbitrary volume Ω. Its variation is controlled through the fluctuations of the flux vector $\boldsymbol{R} = \boldsymbol{u}\boldsymbol{\tau}$ and the scalar source term Q

$$\frac{\partial}{\partial t}\int_{\Omega_l} \boldsymbol{\tau}\,\mathrm{d}\Omega = \oint_{\Gamma} \boldsymbol{R}\cdot\boldsymbol{n}\,\mathrm{d}\Gamma + \int_{\Omega_l} Q\,\mathrm{d}\Omega \tag{10}$$

The core of this cell-vertex fluctuation distribution scheme is to evaluate these two variations on each fv triangle, and to distribute them to the three vertices of the cell according to the preferred strategy. The update of a given node l is obtained by summing the contributions from its control volume, Ω_l, that is composed of all the fv triangles surrounding node l, see Figure 2(c).

When source terms are involved, the standard treatment advocated widely in the literature consists in dealing separately with the flux and the source terms, say in the form

$$\hat{\Omega}_l^{\mathrm{T}}\frac{\boldsymbol{\tau}_l^{n+1} - \boldsymbol{\tau}_l^{n}}{\Delta t} = \alpha_l^{\mathrm{T}} R_{\mathrm{T}} + Q_{\mathrm{MDC_T}}^{l} \tag{11}$$

for a particular triangle T. $\hat{\Omega}_l^{\mathrm{T}}$ is the area of the median dual cell ($\mathrm{MDC_T}$) associated with node l within the triangle T (Figure 2(c)) and the subscripts T and $\mathrm{MDC_T}$ indicate the control volume over which the flux and the source terms are integrated. However, this method has proved itself to be highly inaccurate, even for model viscoelastic problems with non-trivial source terms. This is due to the incompatibility of control volumes between the two contributions and their alternative discretizations [34]. For extensional flows (convection-problems), Wapperom and Webster [12] developed an alternative scheme that consistently distributes both flux and source terms over the fv triangle,

$$\hat{\Omega}_l^{\mathrm{T}}\frac{\boldsymbol{\tau}_l^{n+1} - \boldsymbol{\tau}_l^{n}}{\Delta t} = \alpha_l^{\mathrm{T}}(R_{\mathrm{T}} + Q_{\mathrm{T}}) \tag{12}$$

Note, by design, the LDB scheme *does not impose positivity upon the source terms*. To evaluate the integrals R_{T} and Q_{T}, the velocity and stress were approximated as piecewise linear from the vertices of the fv triangle and the velocity gradients are recovered from the parent fe velocity field (hence, are linear and continuous across the fv sub-cells). This approach, denoted FVL in Reference [12], achieved second-order accuracy at steady state for

sink and Cartesian model problem flows. However, it was necessary to have recourse to the quadratic representation from the parent fe for the velocity and stress (FVQ form of Reference [12]), to maintain second-order accuracy when the flow was nearly parallel to the boundaries (as would arise near no-slip boundaries).

Switching attention from these extensional model problems to pure shear and mixed shear/extensional flows, required two additional strategies to retain stability; consistent streamline-wise upwinding and area integral 'median dual cell' contributions. Hence, Wapperom and Webster proposed the following generalised distribution scheme [26]:

$$\hat{\Omega}_l^{\mathrm{T}} \frac{\boldsymbol{\tau}_l^{n+1} - \boldsymbol{\tau}_l^n}{\Delta t} = \delta_{\mathrm{T}} \alpha_l^{\mathrm{T}} (R_{\mathrm{T}} + Q_{\mathrm{T}}) + \delta_{\mathrm{MDC}} (R^l_{\mathrm{MDC_T}} + Q^l_{\mathrm{MDC_T}}) \tag{13}$$

The parameters δ_{T} and δ_{MDC} are used to discriminate between various update strategies. With $\delta_{\mathrm{T}} = f(We, a, h)$ and $\delta_{\mathrm{MDC}} = 1$, the nodal update is similar to consistent streamline upwinding as used in finite elements. The function f is such that $f = \xi/3$ if $|\xi| \leqslant 3$ and 1 otherwise, where $\xi = We(a/h)$, with a the magnitude of the advection velocity per fv-cell and h the square-root of the area of the fv-cell in question. In this manner, Wapperom and Webster [26] generated solutions for a We_{crit} of 1.5 for smooth flow past a cylinder and 1.3 for the abrupt 4:1 contraction problem, without imposing additional stabilization techniques. This situation was marginally improved upon in the latter instance with momentum strain-rate stabilization, then reaching a critical Weissenberg number of 1.5. Accordingly, we retain this method as the foundation for our present hybrid fe/fv implementation and extended study. The above deliberations have emphasized the importance of treating the contributions from the flux and source terms in a consistent manner. Therefore, we proceed to extend such considerations to the time terms, following Hubbard and Roe [35] for pure convection problems. Equation (13) for a single triangle update, is labelled scheme CT_0: a form that lacks time consistency, due to area weighting. The complete nodal update corresponds to the sum of the contributions from all triangles surrounding the node (see Figure 2(c)), defining $\hat{\Omega}_l$ as the area of the MDC associated with node l.

To enforce consistency, the contribution from the triangles (upon which the fluctuation distribution scheme impinges) and that from the MDC (distributed uniformly) may be weighted with an appropriate area and then summed to yield the nodal update, viz.

$$\frac{\boldsymbol{\tau}_l^{n+1} - \boldsymbol{\tau}_l^n}{\Delta t} = \frac{\sum_{\forall \mathrm{T}} \delta_{\mathrm{T}} \alpha_l^{\mathrm{T}} (R_{\mathrm{T}} + Q_{\mathrm{T}})}{\hat{\Omega}_{\mathrm{FD}}} + \frac{\sum_{\forall \mathrm{T}} (R^l_{\mathrm{MDC_T}} + Q^l_{\mathrm{MDC_T}})}{\hat{\Omega}_l} \tag{14}$$

Here, we introduce two possible options as consistent schemes, dependent upon the area sum $\hat{\Omega}_{\mathrm{FD}} = \sum_{\forall \mathrm{T}} \delta_{\mathrm{T}} \alpha_l^{\mathrm{T}} \Omega_{\mathrm{T}}$, where Ω_{T} is the area of the triangle T. Both schemes follow Equation (14), with exception when $\hat{\Omega}_{\mathrm{FD}}$ falls below a predefined threshold (say 10^{-14}). Under such circumstances, CT_1 reverts to a pure MDC approach (discarding the FD-term); alternatively, CT_2 retains the FD-contribution, by recourse to CT_0, so that then $\hat{\Omega}_{\mathrm{FD}} = \hat{\Omega}_l$.

The motivation for such options lies in the fact that the area sum, dividing the contributions from the triangles Equation (14), can vanish near no-slip boundaries, where the average velocity tends to zero. Indeed, in pure shear flow regions, the velocity is parallel to the walls, and it is our experience that, a pure median dual cell approach is a reasonable choice. Hence, we expect CT_1 to be more accurate than CT_0 in the shear flow zones of the 4:1

contraction problem. However, in the immediate vicinity of the corner, where the flow is mainly extensional, one needs to retain the information from the fluctuation distribution term as well. This is the rationale upon which we have constructed scheme CT_2, which is superior to CT_1. Findings suggest that oscillations beyond the corner, arising as a consequence of the sharp local gradient, are significantly smoothed from scheme CT_1 to CT_2 (see Reference [36]).

Other issues that influence trends in solution quality are: the discretization of the stress flux integral (R_T) - conservative/non-conservative; the order of the solution representation - stress linear/quadratic; the order and continuity of gradient approximation; and the quadrature rules used to evaluate the integrals. The combination of these specific options generates the current fv scheme variants, summarized in Table I for mesh M2. This mesh is sufficiently coarse to stimulate discrepancies in solution smoothness across scheme versions, prior to mesh refinement studies. Calibration is performed against the fe/supg scheme, see Reference [1], for which We_{crit} is 4.1 on mesh M2.

Scheme FV0, with *quadratic stress* interpolation, reached the modest level of We_{crit} of 1.1. This was disappointing, following the promising performance of FV0 on the smooth flow of an Oldroyd-B fluid past a cylinder in an infinite domain [26]; there, We_{crit} reached 1.5, surpassing that for fe/supg of 1.4. In the 4:1 contraction flow, FV0 solutions match the fe/supg counterparts almost exactly in core flow; FV0 stress, τ_{xx}, suffers from oscillations, along the downstream wall just beyond the re-entrant corner.

Linear interpolation of all primary variables was successfully utilised in the fe-context by Basombrío *et al.* [25]. With this in mind, we propose the *linear stress* representation of scheme FV1, that stimulated an advance in stability response, elevating We_{crit} from 1.1 for FV0 to 1.6 with scheme FV1. With FV1, the amplitude of post-corner oscillations is reduced; there, the undershoot capture is better; the solution is shifted towards, though remains slightly out of phase with, the fe/supg representation. Time consistency, as above, improved We_{crit} levels to 1.7, for CT_1 (FV1.1), and 2.0 for CT_2 (FV1.2). The phase lag, common to FV0 and FV1 family schemes, is attributed to the dissipative nature of line-integral stress-flux approximation (standard to most fv-schemes).

Non-conservative *area integration* of R_T (with stress-gradient evaluation) leads to schemes FV2 and above. Scheme FV2.1, with linear stress, is most promising: at $We = 0.5$ it removes the phase-lag and sharpens the post-corner τ_{xx}-profile on the downstream wall, above and beyond both line-integral (FV1.2) and fe/supg alternatives. Additionally, FV2.1 produces the most accurate fully-developed exit (shear) flow achieved with a linear stress representation, both in smoothness and magnitude. Unfortunately, FV2.1 over-estimates the τ_{xx}-peak at the corner, that restricts We_{crit} to 0.8. Such retardation is even more excessive with quadratic stress representation (FV2), to merely 0.3.

To address these large stress peaks (of FV2.1) within the corner neighbourhood, we have implemented scheme FV3, with a *non-recovered, constant stress-gradient*, *multi-valued* from sub-cell to sub-cell. In Figure 3 at $We = 0.8$, we compare the recovered (FV2.1) and non-recovered stress gradient versions (FV3). This corresponds to the maximum attainable *We*-level for the recovered form. The comparison indicates that the corner FV3 stress-peak is lowered, by about one half, tallying with the fe/supg solution (Figure 3(a)). With FV2.1, there are oscillations present, in the less dominant τ_{xy} and τ_{yy} components, prior to the corner. These are removed with scheme FV3. Of major significance is the impact on stability: by imbuing the area integral with multi-valued stress-gradients, We_{crit} *is raised from* 0.8 *to* 3.0. We associate this elevation with enhanced accuracy, leading to improved stability properties.

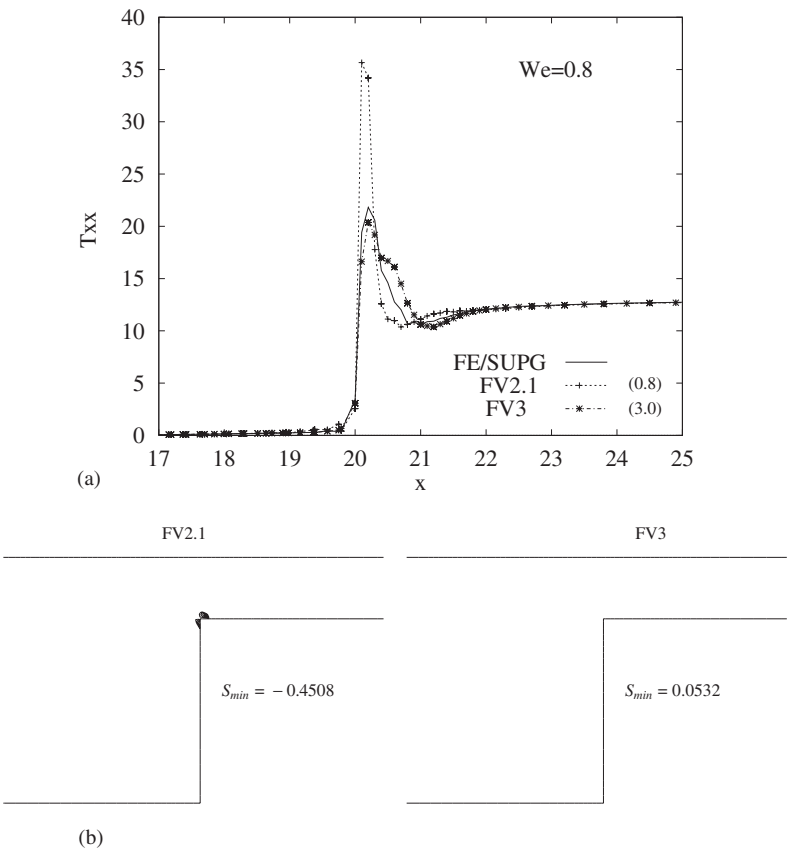

Figure 3. Effect of non-recovered stress gradient: linear stress, Area R_T, CT_2, Corner region; Single-valued stress gradient (FV2.1), Multi-valued (FV3), mesh M2. (a) τ_{xx}-stress line profile $y = 3.0$, fe/supg, FV2.1 and FV3; (b) Steady-state negative S, $We = 0.8$; 11 contours between -1 and 0.

In Figure 3(b), the respective field plots of condition number S (see below for definition) reveal that scheme FV3 has repaired the 'loss of evolution' apparent with FV2.1.

Nevertheless, post-corner stress-profiles of FV3, retain some slight discrepancy from the smoother fe/supg solution. Hence, from a *linear recovered* (continuous), *velocity-gradient* representation in FV3, with scheme FV4 we adopt a *quadratic recovered* form, mimicking that employed in the fe/supg implementation [1]. Except for the corner stress peak value itself, the result is a close match between FV4 and fe/supg profiles. The downside is a reduction in We_{crit} from 3.0 to 2.4 for the FV4 scheme, attendant with elevation of the peak stress value.

At this juncture, we identify the fv-treatment of the corner-solution itself, as being associated with lack-lustre levels of attainment of We_{crit}. This is manifest through the underestimation of τ_{yy} prior to the corner, falling to negative values as we increase elasticity. The contraction flow displays discontinuous corner solutions in stress and velocity-gradient fields. These we may incorporate into the fv-approximation through reduced quadrature for flux and source term integrals. In scheme FV4.1, we adjust our fv quadrature rule, exact for cubics, to a linear

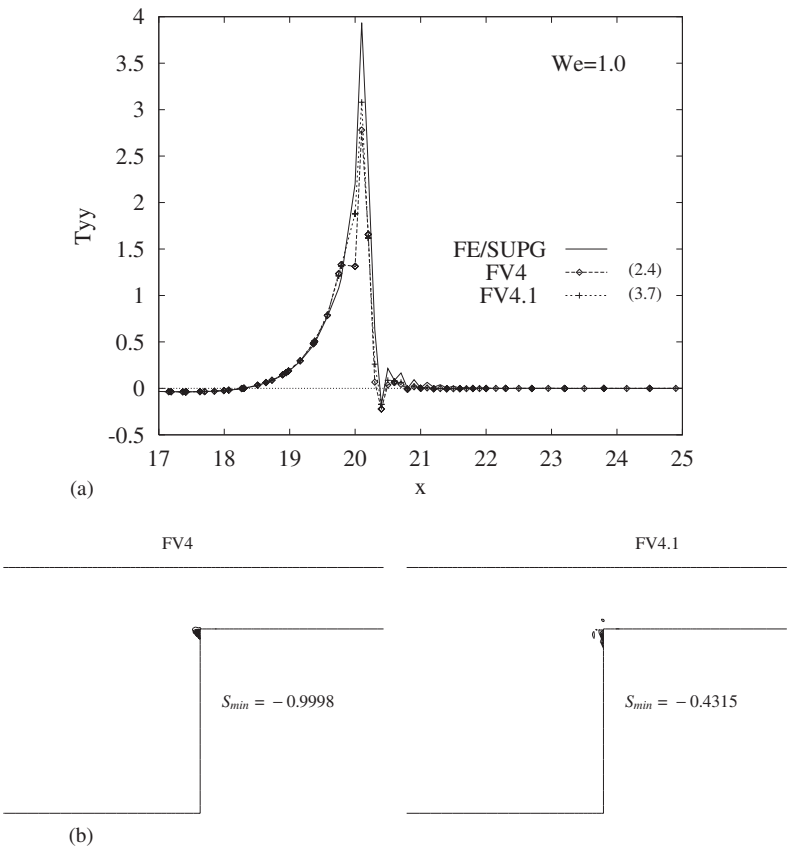

Figure 4. Effect of local corner reduced integration (C.R.I.): FV4 (without C.R.I.) vs. FV4.1 (with C.R.I), mesh M2. (a) τ_{yy}-stress line profile along $y = 3.0$, fe/supg versus (FV4 and FV4.1); (b) Steady-state negative S, $We = 2.4$; 11 contours between -1 and 0.

form within the control volume surrounding the re-entrant corner. Corner reduced integration (C.R.I) has the effect of sampling the integrand, in such a manner, as to be equivalent to adopting a lower order representation of this quantity from cell to cell. Figure 4(a) illustrates how this local treatment brings FV4.1 stress-profiles ($\boldsymbol{\tau}_{xx}$ and $\boldsymbol{\tau}_{yy}$), into line with those of the fe/supg scheme. Scheme FV4.1 corrects the underestimated value of $\boldsymbol{\tau}_{yy}$ at the corner. This, in turn, has increased We_{crit} from 2.4 for scheme FV4, to 3.7 for scheme FV4.1, closely approximating that for the fe/supg scheme of 4.1 on mesh M2. We note below on the refined mesh NM3, that FV4.1 both surpasses fe/supg in stability and provides superior localised solution properties within the stress boundary layers. These layers build up conspicuously along the downstream-wall. The position on condition number S is reflected in Figure 4(b). At We of 2.4, FV4.1 over FV4, is shown to halve the minimum negative level of S, along with the number of nodes infected.

To summarize, an optimal fe/fv hybrid implementation is that of scheme FV4.1. Its attributes are: a linear representation of the stress, based on the fv sub-cell with a non-recovered

(multi-valued) constant stress-gradient; velocity gradients of recovered quadratic form over the parent fe; non-conservative area integrals for R_T, coupled with multi-valued stress-gradients; consistent time-term and reduced integration treatment of re-entrant corner solution gradients. Beyond this point, hybrid combination schemes may also be considered, but await further, more detailed investigation.

5. MESH REFINEMENT

We proceed to demonstrate that FV4-level schemes not only compare favourably with the recent literature, but also highlight some fresh features.

5.1. Vortex behaviour

Adopting the format and conventions of Matallah *et al.* [1], Figure 5 displays the streamlines on mesh M2 for scheme FV4.1 with increasing Weissenberg number. Mesh M2 is the standard mesh employed for the scheme development work (see Reference [36]), and is less refined than that to follow. Both fv schemes provide practically identical solution patterns up to $We < 2$. A lip-vortex is apparent for $We > 1$, with significant lip-vortex growth upon increase of elasticity. For constant viscosity fluids, such behaviour is widely reported in the literature in the same range of Weissenberg number and at comparable levels of mesh size (see References [1, 13, 14, 37, 38]). We go on to note that such lip-vortex growth is spurious (see below), at least up to levels of $We = 2$. From Table I, we observe that We_{crit} levels on mesh M2 equate to 2.4 for scheme FV4 and 3.7 for scheme FV4.1, illustrating the stability enhancement in the

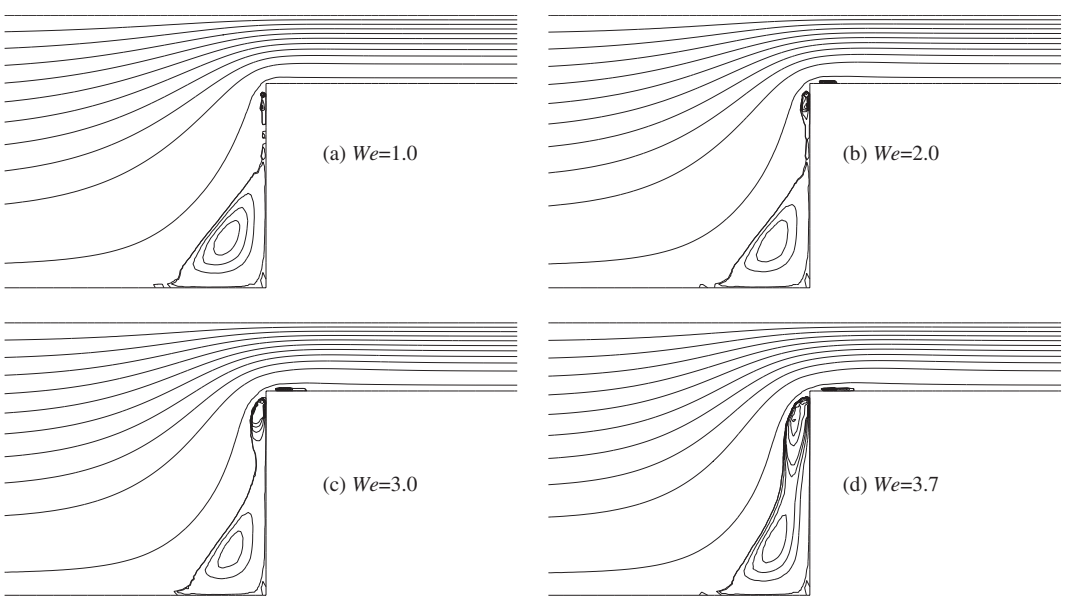

Figure 5. Streamlines with increasing *We*. Scheme FV4.1; Mesh M2.

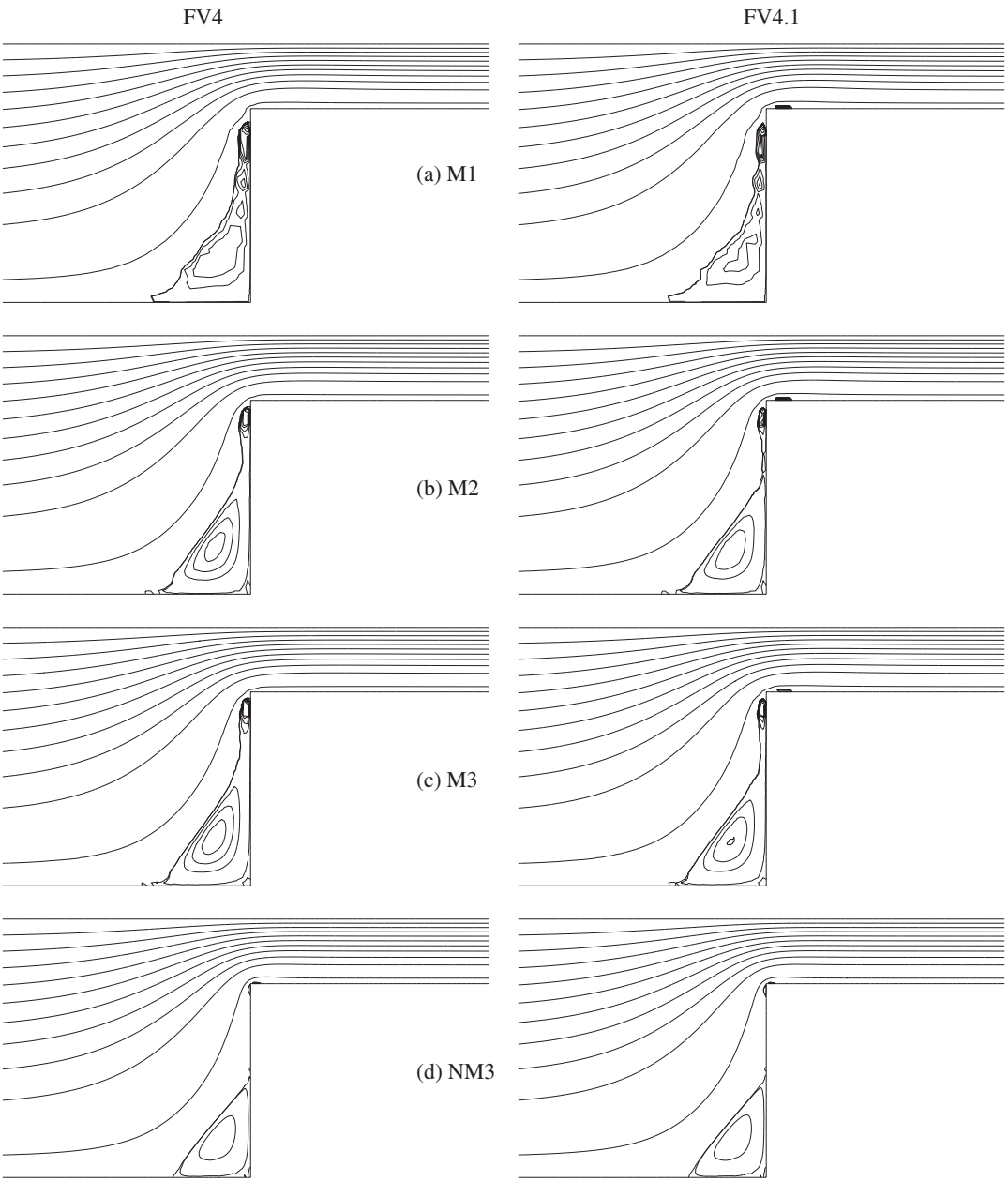

Figure 6. Streamlines with mesh refinement. $We = 2.0$.

latter result. Similar vortex structure to that of Figure 5(d) was reported by Carew *et al.* [27], for a linear PTT model at $We = 10$ and $Re = 1$, with equal-sized lip- and salient-corner vortices.

Mesh refinement is considered in Figure 6 for the four meshes employed. Streamlines patterns are displayed at the larger value $We = 2$ for both fv schemes, FV4 and FV4.1. Here,

Table II. Mesh characteristics.

Meshes	Elements	Nodes	Degrees of freedom $\boldsymbol{u}$, p, $\boldsymbol{\tau}$	$R_{\min}$	Corner element densities Salient	Re-entrant
M1	980	2105	11088	0.024	28	75
M2	1140	2427	12779	0.023	63	85
M3	1542	3279	17264	0.019	135	87
NM3	2987	6220	32717	0.011	201	398

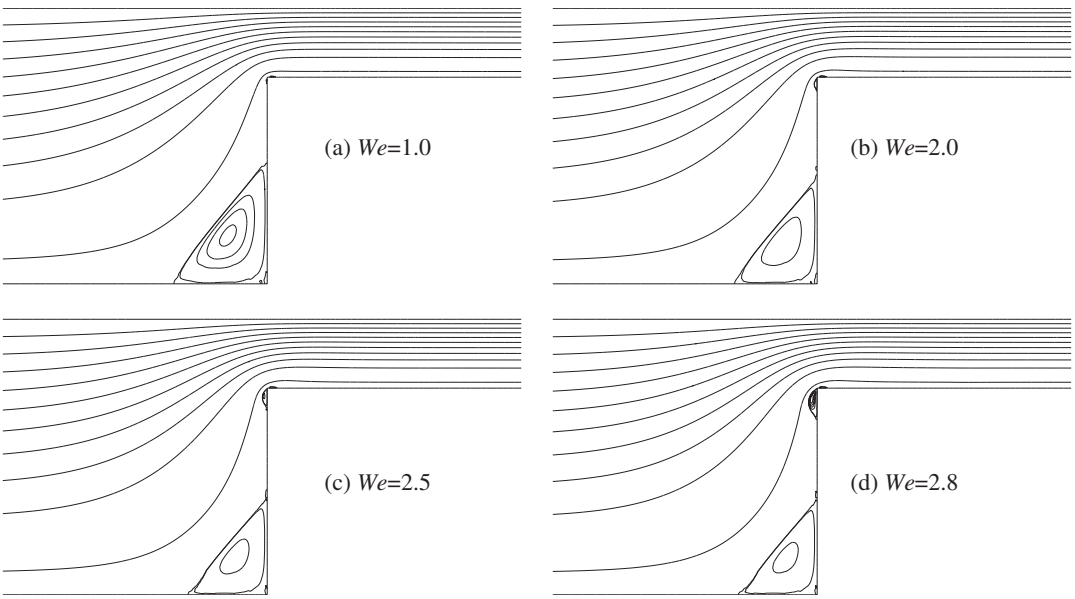

Figure 7. Streamlines with increasing We. Scheme FV4.1; Mesh NM3.

it is apparent that *lip-vortices diminish* and practically vanish at $We = 2$ upon mesh refinement with either fv scheme. This bears out the findings of Matallah *et al.* [1] for Oldroyd-B and Alves *et al.* [14] for an UCM fluid. Solutions on the finest mesh (NM3) display appreciable improvement in solution smoothness over the coarser meshes. A miniscule lip-vortex prevails at this level of fluid elasticity ($We = 2$). Both FV4 and FV4.1 schemes broadly represent the same solution features, and concur on the finest mesh. A faint trailing-edge vortex is detected and scheme FV4.1 points to this even on the coarser meshes (Table II).

These continuous trends are confirmed in Figure 7 with increasing Weissenberg number on our finest mesh, NM3. Both level four schemes give practically identical solutions up to $We = 2.5$, though scheme FV4.1 survives to the larger stability limit of $We = 2.8$. In this respect, the fe/supg scheme is *inferior on finer meshes*, achieving only the modest level of $We = 1.5$, reflecting global pollution in the downstream-wall stress boundary layer solution (see also, Aboubacar *et al.* [28], for illustration on the rounded-corner counterpart problem).

Table III. Lip-vortex intensity (-10^{-3}); (D) numerical divergence, (O) temporal oscillations.

We	Scheme	M1	M2	M3	NM3
1.0	FV4	×	×	×	0.011
	FV4.1	×	×	×	×
1.5	FV4	0.385	0.577	0.697	0.085
	FV4.1	*0.145*	*0.267*	*0.538*	*0.020*
2.0	FV4	1.066	1.272	1.482	0.126
	FV4.1	*0.334*	*0.880*	*1.053*	*0.079*
2.5	FV4	1.578	(D)	(O)	0.177
	FV4.1	*0.420*	*1.365*	*1.773*	*0.286*
2.8	FV4	1.813	(D)	(O)	(D)
	FV4.1	*0.372*	*1.635*	*(D)*	*1.192*

When the mesh is *sufficiently refined*, these fv schemes indicate the persistence of the lip-vortex beyond $We = 2$, say with We of O(3) (see Table III). This is so with/without a discontinuity capturing technique applied at the corner (scheme FV4.1 with; FV4 without): convincing evidence indeed. One must be guarded on this issue, however, as one cannot be categorical without still further mesh refinement. Unfortunately, for the Oldroyd model, further refinement to the corner singularity stimulates stronger stability restrictions and these relatively high levels of elasticity are increasingly more difficult to access (Figure 8).

The existence of a small trailing-edge vortex is confirmed on the downstream wall with rising We, immediately after the re-entrant corner. Such a feature may well have been overlooked by others, even with very refined meshes [13, 14], due to their discretization and griding choices. Nevertheless there is evidence for this in the literature. In the viscous context, Dennis and Smith [39] showed that with considerable mesh refinement, a post-corner trailing-edge vortex was present in the Newtonian case for Reynolds numbers in excess of 150 for flow in a 2:1 contraction geometry. In the viscoelastic regime and for the present problem, Baloch *et al.* [40] hinted at the existence of such a trailing-edge vortex at $We = 5$, for a pseudo-steady-state solution. They incorporated a local discontinuity capturing technique into their Taylor–Galerkin fe/supg implementation (see also Carew *et al.* [41]), following a Galerkin-least-squares approach.

The intensity of the lip-vortex is provided in Table III. It increases with We on each mesh and for both level four schemes. Generally, the finest mesh NM3 provides lowest intensity levels for each scheme. Correspondingly, the strength of the salient-corner vortex is charted in Table IVa. The finest mesh values reflect a gradual decline with increasing We. These trends are in close agreement with those observed by Matallah *et al.* [1], and Alves *et al.* [14].

The salient-corner vortex cell size, (X) (Table IVb), has been reported widely in the literature to remain fairly constant (at around 1.4) with increasing elasticity [1, 11, 13, 15, 37]. The quantity (X), is defined as the length between the salient-corner and the intersecting point of the vortex separation line on the upstream wall. We confirm the constancy of X on the coarser mesh M2 with scheme FV4.1, the identical mesh used to produce the fe/supg results of Matallah *et al.* [1]. In fact, all consistent methods agree with these findings on coarser meshing, as illustrated in Figure 9(a).

In contrast to the above, results on our finest mesh NM3 of Table IV reveal that the size of the salient-corner vortex actually decreases linearly with increasing Weissenberg number.

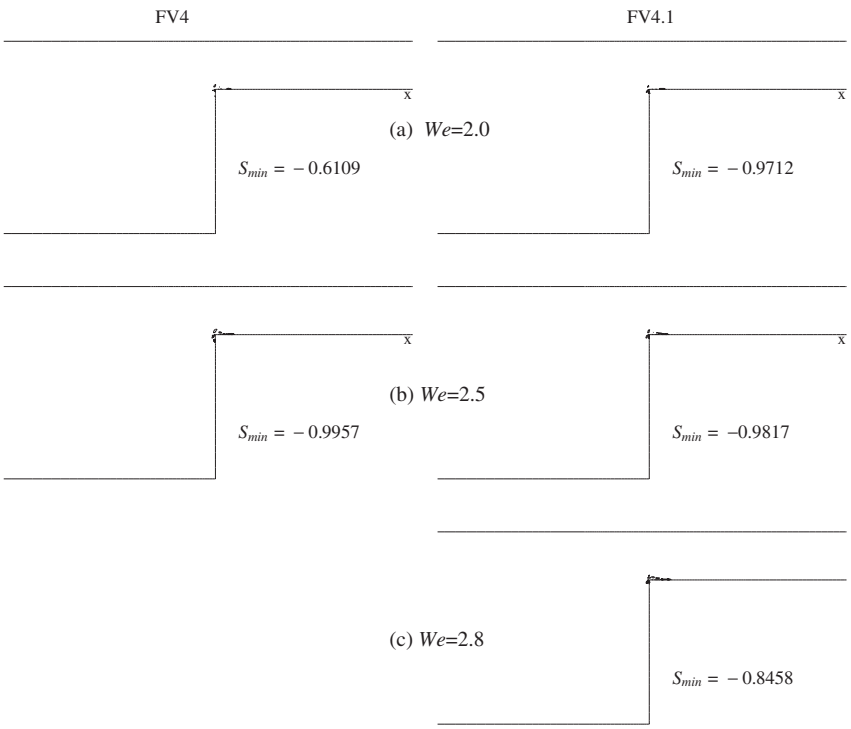

Figure 8. Condition number S with increasing We, mesh NM3.

Figure 9(b) demonstrates satisfactory agreement between FV4.1 (or FV4) on mesh NM3, and the min-mod scheme of Alves *et al.* on their third and fourth finer meshes, both in trends and magnitude (see Table IV for relevant data). On mesh NM3 at $We = 2.8$, 18% reduction in X is observed from the position at $We = 0.1$. Likewise, Alves *et al.* [14] reported a significant decrease in salient-corner cell size for an UCM fluid through consistent mesh refinement (38%, as We was raised from zero to three).

5.2. Stress patterns

Stress contour lines emphasise solution convergence with mesh refinement in the three component stress fields, as provided in Figure 10 at $We = 2$. This confirms scheme FV4.1 convergence on the finest mesh, NM3, showing the contrast to solutions on mesh M2. There is no discernible difference in the patterns in core flow away from the corner and solutions on mesh NM3 are smoothed considerably in the corner region. A clear indication is provided of the build up of boundary layers in $\boldsymbol{\tau}_{xx}$ and $\boldsymbol{\tau}_{xy}$, finely resolved on mesh NM3. The width of stress boundary layers for various models and flows is discussed by Renardy [42], Hagen and Renardy [43], (width of We^{-1} for Oldroyd-B and this flow). The stress fields of Figure 10 are in close correspondence with those of Phillips *et al.* [13]. On our finest mesh NM3 at $We = 2$, and with corner treatment introduced into scheme FV4 producing scheme FV4.1, almost identical patterns are observed in all stress components for both schemes. Only

Table IV. (D) numerical divergence, (O) temporal oscillations.

We	Scheme	M1	M2	M3	NM3
(a) *Salient corner vortex intensity* (-10^{-3})					
0.1	FV4	0.605	0.962	0.989	0.860
	FV4.1	*0.603*	*0.960*	*0.987*	*0.860*
1.0	FV4	0.665	0.956	0.944	0.816
	FV4.1	*0.643*	*0.918*	*0.913*	*0.811*
1.5	FV4	0.687	0.897	0.924	0.647
	FV4.1	*0.614*	*0.807*	*0.850*	*0.645*
2.0	FV4	0.706	0.867	0.921	0.447
	FV4.1	*0.573*	*0.677*	*0.767*	*0.489*
2.5	FV4	0.978	(D)	(O)	0.368
	FV4.1	*0.557*	*0.622*	*0.801*	*0.377*
2.8	FV4	1.256	(D)	(O)	(D)
	FV4.1	*0.581*	*0.610*	*(D)*	*0.350*
(b) *Salient corner vortex cell-size*, X, *across mesh with increasing We*, FV4 *and* FV4.1					
0.1	FV4	1.500	1.400	1.600	1.412
	FV4.1	*1.500*	*1.400*	*1.600*	*1.412*
1.0	FV4	1.500	1.400	1.600	1.358
	FV4.1	*1.500*	*1.400*	*1.600*	*1.358*
2.0	FV4	1.500	1.400	1.500	1.203
	FV4.1	*1.500*	*1.400*	*1.500*	*1.203*
2.8	FV4	1.500	(D)	(O)	(D)
	FV4.1	*1.500*	*1.400*	*(D)*	*1.154*

minor modification in the corner region is apparent with FV4.1. This demonstrates how the local treatment of the re-entrant corner solution is crucial in guaranteeing stability on coarser meshes. It is also essential for accuracy, if finer flow features are to be captured on more refined meshes.

5.3. *Loss of evolution*

The ability of a numerical scheme to retain the evolutionary character of the underlying equation system may be used as a stability indicator for that particular scheme [11, 13, 25, 27, 44, 45]. Dupret and Marchal [46] proposed a criterion to indicate loss of evolution for a Maxwell fluid, via the condition number S,

$$S = 2\frac{s_1 * s_2}{{s_1}^2 + {s_2}^2} \tag{15}$$

where s_1 and s_2, accordingly, are the non-trivial eigenvalues of the tensor $T_A = \boldsymbol{\tau} + (\mu_e/We)I$. With frozen initial and boundary conditions applied, S should remain positive throughout the flow domain to avoid the loss of evolution. Connected regions of such behaviour would be particularly disastrous, that would consequently lead to numerical divergence. Strictly speaking, the theory applies to the strong solution of a Maxwell model in inertial flows. Therefore, in

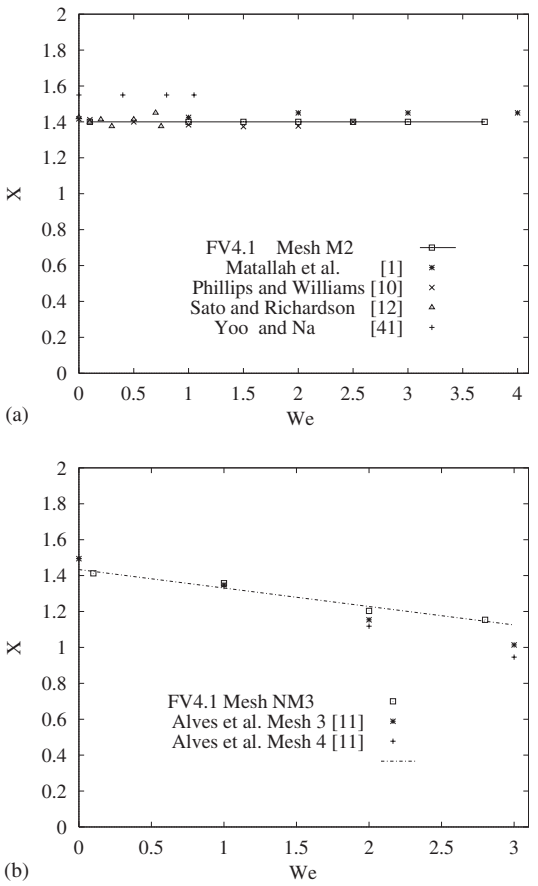

Figure 9. Size of salient corner vortex with increasing We; Scheme FV4.1. (a) Mesh M2; (b) mesh NM3.

the case of the Oldroyd model, the condition number S is only an indicator of failure in scheme evolution, relying upon similar discrete structure.

It is instructive to investigate the relationship between the behaviour of factor S and the appearance of lip and trailing-edge vortices. In Figure 8, we report the condition number on our finest mesh NM3, for schemes FV4 and FV4.1, with increasing We. We comment that for $We < 1$, there is a complete lack of negative values of S. At $We = 1$, there is a single negative value located at the corner. For higher We, isolated sporadic points occur that are restricted to the downstream wall, just beyond the corner. This is strong indication that the appearance of the lip-vortex ($We > 1$, see Figure 7) may trigger the local loss of evolution at isolated points (negative S). The question arises, as to whether it is this resultant loss of evolution that gives rise to the trailing-edge vortex. On the coarser mesh M2 and at $We = 2$, scheme FV4 exhibits a significant lip-vortex without a trailing-edge vortex, while scheme FV4.1 displays both (Figure 6(b)). Nevertheless, field plots for S factor indicate similar polluted zones (only at the lip-vortex) for both schemes. Hence, this alone cannot account for the onset of the trailing-edge vortex.

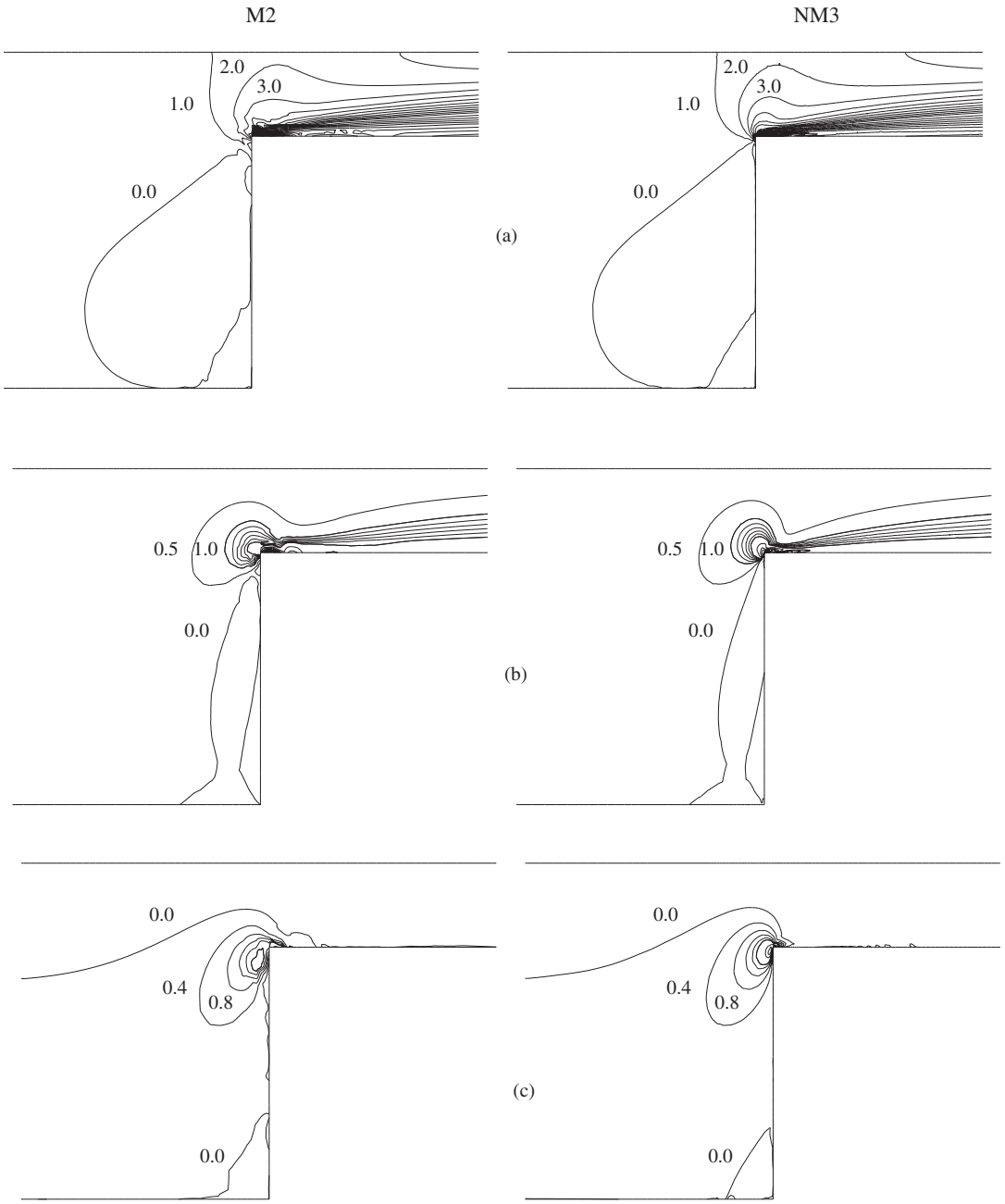

Figure 10. Stress contour lines, $We = 2.0$, FV4.1. (a) τ_{xx}; (b) τ_{xy}; (c) τ_{yy}.

5.4. *Asymptotic behaviour*

The singular asymptotic behaviour of the stress at a re-entrant corner has been studied theoretically by a number of researchers, using an (r,θ) polar coordinate system of reference, centred at the corner [17–19, 47]. For the flow of an Oldroyd-B fluid past a sharp corner and for a given angle θ, Hinch [17] established that velocity components asymptote towards the corner like $r^{5/9}$. In a similar fashion, stress components are singular as $r^{-2/3}$. Hinch assumed the absence of lip-vortices, so that the flow is viscometric near the walls, away from the corner. Renardy [19] subsequently confirmed the findings of Hinch, providing the angle θ is not too small; Renardy [19] also noted that the Hinch formulation violates the momentum equation near the walls.

In this article, we consider two such angles as the solution approaches the corner: $\theta = \pi/2$ and $\theta = \pi$. In this respect, we may restrict ourselves to results for scheme FV4.1, as characteristic of level four schemes. All results illustrate mesh convergence and are plotted for the four meshes at $We = 1$: so prior to lip-vortex onset. At the cross-stream angle ($\theta = \pi/2$), U_r reflects the anticipated theoretical decay, as does $\boldsymbol{\tau}_{rr}$ and $\boldsymbol{\tau}_{r\theta}$ (Figures 11(a) and 11(b)). U_θ and $\boldsymbol{\tau}_{\theta\theta}$ deviate marginally from the predicted slopes, see Figure 11(c) for stress. Similar conclusions were reported by Alves *et al.* [14] for the flow of an UCM fluid. We have observed satisfactory agreement with the theory in all solution components in the upstream direction, ($\theta = \pi$, see Figures 11(d)–(f)). Such agreement is strong confirmation of the high-order of accuracy of present solutions.

6. CONCLUSIONS

We have fashioned a stable and accurate implementation of a novel cell-vertex hybrid finite volume/element scheme, for abrupt planar contraction flow of an Oldroyd-B fluid. This hybrid fe/fv procedure surpasses fe/supg, in stability at high *We* on the more refined meshes, and provides superior representation of stress boundary layers.

A systematic study is conducted for stress behaviour, along a line intersecting the downstream wall. Post-corner oscillations, commonly observed when stresses are calculated at re-entrant corners, are alleviated. This has been achieved via a non-conservative form of the flux, along with a consistent treatment of the transient stress update, and a recovery technique for velocity gradients. Linear stress representation, with non-recovered stress gradients, proved crucial to enhance stability. In addition, we have highlighted the importance of incorporating a local discontinuity capturing technique for the re-entrant corner solution, achieved here via reduced quadrature.

Accuracy has been established in a number of ways: first, we have demonstrated convergence with mesh refinement of salient-corner vortex size and stress fields; second, we have found close agreement with theoretical predictions, in asymptotic behaviour of velocity and stress, approaching the re-entrant corner. Finally, we have shown that our results concur with the literature for the size of the salient-corner vortex. We confirm the existence of a lip-vortex for this problem (for $We > 1$), that grows in size and intensity with increase of *We*. Alternatively, the salient-corner vortex decreases in size and strength with increasing *We*, for such a constant viscosity model. Additionally, we have encountered the existence of a trailing-edge vortex, accompanying the on-set of a lip-vortex. It is clear that the appearance of negative

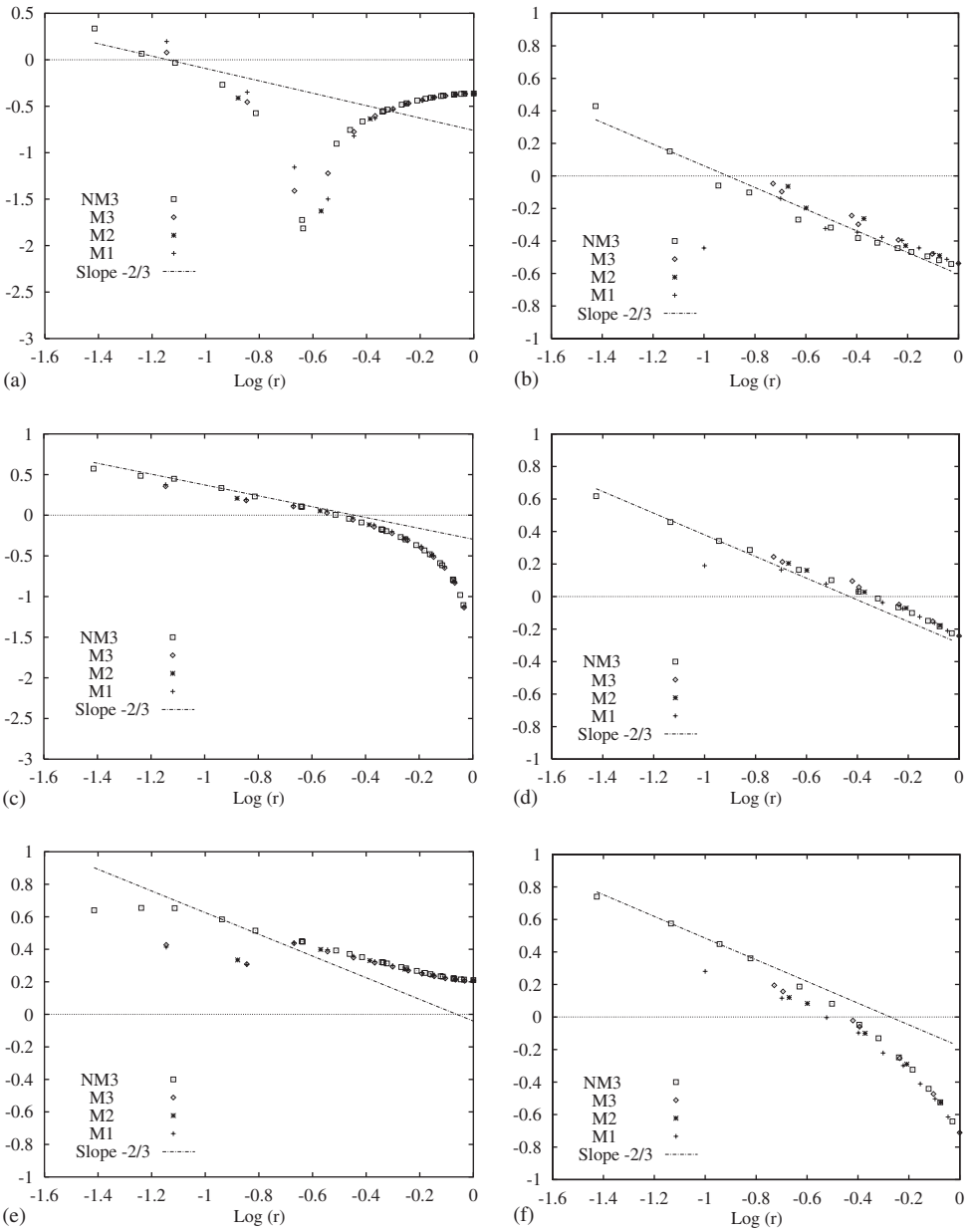

Figure 11. Stress asymptotic behaviour approaching re-entrant corner, along directions $\theta = \pi/2$ (cross-stream) and $\theta = \pi$ (upstream), FV4.1, $We = 1.0$.

values in the condition number S correlates with the presence of a lip-vortex. There is no evidence to suggest that these highly localised negative S values are associated with trailing-edge vortex activity.

Here, the use of the Oldroyd-B model has allowed a measure of scheme performance to be established in terms of stability. There is no doubt that the presence of a re-entrant corner has been all-important in providing the sharpness of solution to distinguish the independent properties of the proposed scheme combinations. In a sequel on contraction flows [28], we proceed to consider three important issues. First, we remove uncertainty associated with the corner singularity and round the corner, to produce smooth flows, with a complex mix of shear and extension. Second, we retain the Oldroyd-B model, to assess stability and to make direct comparison between rounded and abrupt corner flows. Lastly, we have recourse to Phan–Thien–Tanner constitutive models (linear and exponential), to consider alternative forms of material rheology. This introduces shear-thinning and strain-softening/hardening properties. Accordingly, attainable levels of elasticity are raised, to an order of magnitude beyond that realised for the Oldroyd-B model. The proposed hybrid fe/fv scheme, armed with its identified and attractive properties of efficiency, accuracy and stability, awaits further validation in more complex scenarios. In the future, we intend to investigate time-dependent flows, high-order fluctuation distribution schemes, free-surface problems, three-dimensional flows and the extreme conditions identified in industrial processing.

REFERENCES

1. Matallah H, Townsend P, Webster MF. Recovery and stress-splitting schemes for viscoelastic flows. *Journal of Non-Newtonian Fluid Mechanics* 1998; **75**:139–166.
2. Matallah H. *Ph.D. Thesis*, University of Wales, Swansea, 1998.
3. White SA, Gotsis AD, Baird DG. Review of the entry flow problem: experimental and numerical. *Journal of Non-Newtonian Fluid Mechanics* 1987; **24**:121–160.
4. Baaijens FTP. Mixed finite element methods for viscoelastic flow analysis: a review. *Journal of Non-Newtonian Fluid Mechanics* 1998; **76**:361.
5. Walters K, Webster MF. The distinctive CFD challenges of computational rheology. *ECCOMAS 2001*, *International Journal for Numerical Methods in Fluids* 2003; in press.
6. Morton KW, Paisley MF. A finite scheme with shock fitting for the steady Euler equations. *Journal of Computational Physics* 1989; **80**:168–203.
7. Crumpton PI, MacKenzie JA, Morton KW. Cell-vertex algorithms for the compressible Navier–Stokes equations. *Journal of Computational Physics* 1993; **109**:1–15.
8. Struijs R, Deconinck H, Roe PL. Fluctuation splitting for the 2D Euler equations. *Technical Report* 1990-01. Von Karman Institute for Fluid Dynamics, 1991.
9. Tomaich GT, Roe PL. Compact schemes for advection diffusion problems on unstructured grids. *Modelling Simulation* 1993; **23**:2629.
10. Berzins M, Ware JM. Positive cell-centred finite volume discretisation methods for hyperbolic equations on irregular meshes. *Applied Numerical Mathematics* 1995; **16**:417–438.
11. Marchal JM, Crochet MJ. A new mixed finite element for calculating viscoelastic flow. *Journal of Non-Newtonian Fluid Mechanics* 1987; **26**:77–114.
12. Wapperom P, Webster MF. A second-order hybrid finite-element/method for viscoelastic flows. *Journal of Non-Newtonian Fluid Mechanics* 1998; **79**:405–431.
13. Phillips TN, Williams AJ. Viscoelastic flow through a planar contraction using a semi-Lagrangian finite volume method. *Journal of Non-Newtonian Fluid Mechanics* 1999; **87**:215–246.
14. Alves MA, Pinho FT, Oliveira PJ. Effect of a high-resolution differencing scheme on finite-volume predictions of viscoelastic flows. *Journal of Non-Newtonian Fluid Mechanics* 2000; **93**:287–314.
15. Sato T, Richardson SM. Explicit numerical simulation of time-dependent viscoelastic flow problems by a finite element/finite volume method. *Journal of Non-Newtonian Fluid Mechanics* 1994; **51**:249–275.
16. Xue S-C, Phan-Thien N, Tanner RI. Three dimensional numerical simulations of viscoelastic flows through planar contractions. *Journal of Non-Newtonian Fluid Mechanics* 1998; **74**:195–245.
17. Hinch EJ. The flow of an Oldroyd fluid around a sharp corner. *Journal of Non-Newtonian Fluid Mechanics* 1993; **50**:161–171.
18. Renardy M. The stresses of an upper convected Maxwell fluid in a Newtonian velocity field near a re-entrant corner. *Journal of Non-Newtonian Fluid Mechanics* 1993; **50**:127–134.
19. Renardy M. A matched solution for corner flow of the upper convected Maxwell fluid. *Journal of Non-Newtonian Fluid Mechanics* 1995; **58**:83–89.

20. Xue S-C, Phan-Thien N, Tanner RI. Numerical study of secondary flows of viscoelastic fluid in straight pipes by an implicit finite method. *Journal of Non-Newtonian Fluid Mechanics* 1995; **59**:191–213.
21. Huang X, Phan-Thien N, Tanner RI. Viscoelastic flow between eccentric rotating cylinders: unstructured control volume method. *Journal of Non-Newtonian Fluid Mechanics* 1996; **64**:71–92.
22. Baaijens FPT. Application of low-order discontinuous Galerkin method to the analysis of viscoelastic flows. *Journal of Non-Newtonian Fluid Mechanics* 1994; **52**:37–57.
23. Baaijens FPT. An iterative solver for the DEVSS/DG method with application to smooth and non-smooth flows of the upper convected Maxwell fluid. *Journal of Non-Newtonian Fluid Mechanics* 1998; **75**:119–138.
24. Fortin M, Fortin A. A new approach for the fem simulation of viscoelastic flows. *Journal of Non-Newtonian Fluid Mechanics* 1989; **32**:295–310.
25. Basombrío FG, Buscaglia GC, Dari EA. Simulation of highly elastic fluid flows without additional numerical diffusivity. *Journal of Non-Newtonian Fluid Mechanics* 1991; **39**:189–206.
26. Wapperom P, Webster MF. Simulation for viscoelastic flow by a finite volume/element method. *Computer Methods in Applied Mechanics and Engineering* 1999; **180**:281–304.
27. Carew EOA, Townsend P, Webster MF. A Taylor–Petrov–Galerkin algorithm for viscoelastic flow. *Journal of Non-Newtonian Fluid Mechanics* 1993; **50**:253–287.
28. Aboubacar M, Matallah H, Webster MF. Highly Elastic Solutions for Oldroyd-B and Phan-Thien/Tanner Fluids with a Finite Volume/Element Method: planar contraction flows. *Journal of Non-Newtonian Fluid Mechanics* 2002; **103**:65–103.
29. Carew EOA, Townsend P, Webster MF. Taylor–Galerkin algorithms for viscoelastic flow: application to a model problem. *Journal of Numerical Methods for PDE* 1994; **10**:171–190.
30. Zienkiewicz OC, Morgan K, Peraire J, Vandati M, Löhner R. Finite elements for compressible gas flow and similar systems. In *7th International Conference on Computer Methods in Applied Science and Engineering*, Versailles, France, 1985.
31. Donea J. A Taylor–Galerkin method for convective transport problems. *International Journal for Numerical Methods in Engineering* 1984; **20**:101–119.
32. Van Kan J. A second-order accurate pressure-correction scheme for viscous incompressible flow. *SIAM Journal of Scientific and Statistical Computing* 1986; **7**(3):870–891.
33. Hawken DM, Tamaddon-Jahromi HR, Townsend P, Webster MF. A Taylor–Galerkin based algorithm for viscous incompressible flow. *International Journal for Numerical Methods in Fluids* 1990; **10**:327–351.
34. Chandio MS, Webster MF. On consistency of cell-vertex finite formulations for viscoelastic flow. In *XIII International Congress on Rheology*, vol. 2, Cambridge, UK, 2000; 2–208.
35. Hubbard ME, Roe PL. Multidimensional upwind fluctuation distribution schemes for scalar time dependent problems. *Numerical Analysis Report* 1/98, Department of Mathematics, University of Reading, 1998.
36. Aboubacar M, Webster MF. Development of an optimal hybrid finite volume/element method for viscoelastic flows. *Under review*, *International Journal for Numerical Methods in Fluids*, available as CSR15-2000. University of Wales, Swansea, 2000.
37. Yoo JY, Na Y. A numerical study of the planar contraction flow of a viscoelastic fluid using the SIMPLER algorithm. *Journal of Non-Newtonian Fluid Mechanics* 1991; **39**:89–106.
38. Marchal JM, Crochet MJ. Hermitian finite elements for calculating viscoelastic flow. *Journal of Non-Newtonian Fluid Mechanics* 1986; **20**:187–207.
39. Dennis SCR, Smith FT. Steady flow through a channel with a symmetrical constriction in the form of a step. *Proceedings of the Royal Society of London* 1980; **A327**:393.
40. Baloch A, Carew EOA, Townsend P, Webster MF. A Taylor–Petrov–Galerkin algorithm for viscoelastic flow. *Report CSR* 14-93, University of Wales, Swansea, 1993.
41. Carew EOA, Townsend P, Webster MF. On a discontinuity capturing technique for Oldroyd-B fluids. *Journal of Non-Newtonian Fluid Mechanics* 1994; **51**:231–238.
42. Renardy M. High Weissenberg boundary layers for the upper convected Maxwell fluid. *Journal of Non-Newtonian Fluid Mechanics* 1997; **68**:125–132.
43. Hagen T, Renardy M. Boundary layer analysis of the Phan-Thien-Tanner and Giesekus model in high Weissenberg number flow. *Journal of Non-Newtonian Fluid Mechanics* 1997; **73**:181–189.
44. Dupret F, Marchal JM, Crochet MJ. On the consequence of discretization errors in the numerical calculation of viscoelastic flow. *Journal of Non-Newtonian Fluid Mechanics* 1985; **18**:173–186.
45. Luo X-L, Tanner RI. A decoupled finite element streamline-upwind scheme for viscoelastic flow problems. *Journal of Non-Newtonian Fluid Mechanics* 1989; **31**:143–162.
46. Dupret F, Marchal JM. Sur le signe des valeurs propres du tenseur des extra-contraintes dans un écoulement de fluide de Maxwell. *Journal de Mécanique Théorique et Appliquée* 1986; **5**:403–427.
47. Tanner RI, Huang X. Stress singularities in non-Newtonian stick-slip and edge flows. *Journal of Non-Newtonian Fluid Mechanics* 1993; **50**:135–160.

